PCCP

PAPER

View Article Online
View Journal | View Issue

Check for updates

Cite this: *Phys. Chem. Chem. Phys.*, 2020, **22**, 22302

Selective bond formation triggered by short optical pulses: quantum dynamics of a four-center ring closure†

Alessio Valentini,‡ Stephan van den Wildenberg and F. Remacle *

Received 26th June 2020,
Accepted 23rd September 2020

DOI: 10.1039/d0cp03435e

rsc.li/pccp

We report bond formation induced by an ultrashort UV pulse. The photochemical process is described by quantum dynamics as coherent electronic and nuclear motions during the ultrashort pulse induced ring closure of norbornadiene to quadricyclane. Norbornadiene consists of two ethylene moieties connected by a rigid $(CH_2)_3$ bridge. Upon photoexcitation, two new sigma bonds are formed, resulting in the closure of a four-atom ring. As a medium-sized polyatomic molecule, norbornadiene exhibits a high density of strongly coupled electronic states from about 6 eV above the ground state. We report on inducing the formation of the new bonds using a short femtosecond UV pulse to pump a non-equilibrium electronic density in the open form that evolves towards the closed ring form. As the coherent electronic-nuclear coupled dynamics unfold, the excited states change character through non-adiabatic interactions and become valence states for the two new C–C bonds of quadricyclane. Our three-dimensional fully quantum dynamical grid simulations during the first 200 fs show that short UV pulses of different polarization initiate markedly different initial non-equilibrium electronic densities that follow different dynamical paths to the S_0/S_1 conical intersection. They lead to different initial relative yields of quadricyclane, thereby opening the way to controlling bond-making with attopulses.

Published on 24 September 2020. Downloaded on 1/26/2021 11:44:03 AM.

Introduction

The development of controlled ultrashort sub-femtosecond[1,2] and few femtosecond (fs)[3–5] optical pulses allows manipulating electronic densities in molecules in space and in time.[6–10] Several experimental and computational studies reported using such pulses to steer the vibronic dynamics in the excited states to fragmentation products.[11–18] Here, we demonstrate how to use short UV pulses to selectively make bonds. We investigate quantum dynamically the photoisomerization of norbornadiene to quadricyclane induced by short few fs linearly polarized UV pulses. Pericyclic reactions are the prototype of reaction mechanisms based on transferring localized electronic densities from old bonds to new ones. This process requires a concerted motion of electrons and nuclei. The ring closure of norbornadiene to quadricyclane presents several appealing features. First, the reaction takes place with relatively small nuclear displacements, as the two double bonds are locked in place by the carbon bridge. Second, the electrons play a central role in the reaction, which can be exploited by tuning an external optical pulse to create the coherent superposition of electronic excited states that leads efficiently to the product.

Photoinduced pericyclic reactions are typically triggered by exciting a single electronic state. The vibronic wave packet on this state evolves to the product through conical intersections that bring about the change of electron configuration required to reach the product region on the ground electronic state.[19–24] Typically, the main conical intersection involves an asymmetric distortion of the open form geometry and occurs at geometries far from that of the Franck–Condon region. The rather long time scales that were reported for the photoisomerization process, of the order of dozens of fs, reflect the time it takes for the vibronic wave packet on the excited electronic state to travel to the conical intersection region. Pioneering studies of these fast processes used fs to sub ps pump–probe set-ups, see for example.[25–33] Starting from a single excited state, the wave packet often propagates through several conical intersection regions before reaching the products. The time scales can be inferred from the study of critical points on the potential energy surface.[22,30] Dynamical simulations were also used such as surface hopping,[34–37] semiclassical hybrid-quantum methods[38–40] or quantum methods such as MCTDH[41,42] or based on grid representations.[43–45]

A short few fs's pulse can build a coherent superposition of several excited electronic states that can be of Rydberg or

Theoretical Physical Chemistry, RU MOLSYS, University of Liege, B4000 Liege, Belgium. E-mail: Fremacle@uliege.be

† Electronic supplementary information (ESI) available. See DOI: 10.1039/d0cp03435e

‡ Present address: Department of Chemistry, Standford University, CA 94305, USA.

This journal is © the Owner Societies 2020

Published on 24 September 2020. Downloaded on 1/26/2021 11:44:03 AM.

valence or mixed Rydberg/valence character.[15] In this paper, we investigate how few fs linearly polarized UV pulses can be used to control the [2+2] photocycloaddition of norbornadiene (C_7H_8, bicyclo[2.2.1]hepta-2,5-diene). Like most medium-sized polyatomic molecules, norbornadiene exhibits a rather high density of electronic states just above the first excited state, that converge to the ionization potential. These states are strongly coupled by numerous non-adiabatic interactions that modify their character when going from the 'open' norbornadiene isomer to the 'closed' quadricyclane. Higher excited states that have a strong Rydberg character in the Franck–Condon region of norbornadiene become lower excited states in the product region with a valence character on the two new bonds.[32,46,47] These states have been shown experimentally to be essential for the reverse reaction, the photoisomerization of quadricyclane to norbornadiene.[33] Moreover, these high excited states are of definite symmetry in the Franck–Condon region and respond differently to an electric field linearly polarized along different directions.

We show that excitation of oriented norbornadiene by few fs UV pulses with a different direction of polarization allows tailoring the initial non-equilibrium electronic density and obtaining considerably different coherent superpositions of electronic states in the Franck–Condon region with specific Rydberg character. The spatial and temporal localization of the corresponding nuclear wave packets on the excited electronic states follow different paths to bring electronic density between the carbons involved in the formation of the new C–C bonds leading to quadricyclane. In particular, the coherent excitation of higher excited electronic states allows approaching the main S_0/S_1 conical intersection from a region that is not accessible when the excitation is confined to the S_1 state, leading to more efficient conversion to the quadricyclane product when the wave packet crosses the S_0/S_1 conical intersection region. These different paths are drawn schematically in Fig. 1. In the last section of this paper, we show how to monitor the ring closure by computing pump–probe transient absorption spectra along the evolution of the wave packet dynamics.

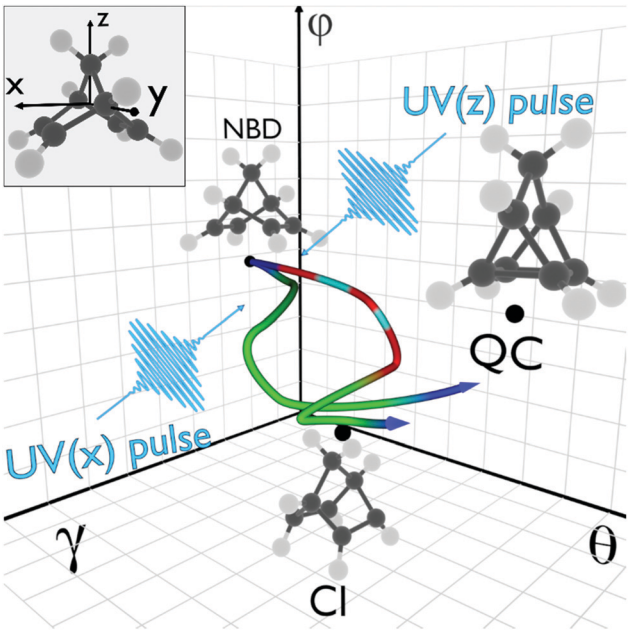

Fig. 1 Cartoon of the two different paths followed by the multi electronic state vibronic wave packets upon excitation of an oriented norbornadiene molecule by a short few fs UV pulse in the reduced system of three coordinates (θ, γ, φ) chosen to describe the early steps of photoisomerization process (see Fig. 2 and text for the definition of the coordinate system, the orientation of the Cartesian frame used throughout is shown as an inset). The pulse is either polarized perpendicularly to the ethylene double bonds (UV(x) pulse), or perpendicularly to the 4C plane (UV(z) pulse). The color shows the changes in the electronic state composition of the vibronic wave packet as it travels to the S_0/S_1 conical intersection (CI) region. Inset: Orientation of norbornadiene (NBD) in the laboratory frame. The UV(x) pulse builds a superposition of the S_1 (green) and S_0 (blue) states in the Franck–Condon region. The S_1 wave packet involves to the S_0/S_1 with essentially no interactions with the other electronic states. The UV(z) pulse builds a coherent superposition of the S_0 (blue) and S_2 (red) states in the Franck–Condon region. The S_2 state is strongly coupled by non adiabatic coupling to the S_3 (turquoise) state. The S_2/S_3 wave packet reaches the S_1 state *via* the S_2/S_1 conical intersection seam in a location around the S_1/S_0 seam completely different from the S_1 wavepacket that results from excitation by the UV(x) pulse. As a result, the initial transfer to the quadricyclane (QC) region on S_0 is larger for the UV(z) excitation than from the UV(x) one.

Computational details

We aim to steer the coherent vibronic dynamics of high mixed Rydberg-valence states from norbornadiene to quadricyclane by building different initial non-equilibrium electronic densities with the pump pulse. We compute the dynamics by integrating the time-dependent Schrödinger equation for eight coupled electronic states of valence and Rydberg character below the ionization potential for a three dimensional grid. The time-dependent amplitudes, $c_{ig}(t)$, where i is the index of an electronic state and g a grid point allow to compute all the observables discussed below.

Three-dimensional coupled electronic dynamics

Pericyclic reactions take place through a correlated motion of electrons and nuclei. As the ring-closure mechanism involve non-adiabatic interactions, it is essential to use quantum methods to compute the dynamics accurately. However, it is not feasible with present days computers and methodologies to treat the electron-nuclear dynamics quantum mechanically in its full dimensionality. Norbornadiene (C_7H_8) has 39 internal nuclear degrees of freedom. In addition, in order to investigate the role of high Rydberg states in the dynamics, several optically accessible electronic states need to be included. Computing the quantum dynamics of the ring-closure process thus requires to identify the most relevant coordinates. Reducing the number of nuclear degrees of freedom allows both efficiently representing the ring-closure process and making the computation tractable, which requires a physical intuition on the reaction mechanism. Such an insight on the mechanism could be gained from 'on the fly' semiclassical approaches like surface hopping or trajectory guided nuclear basis methods. Here, we reduced the

Published on 24 September 2020. Downloaded on 1/26/2021 11:44:03 AM.

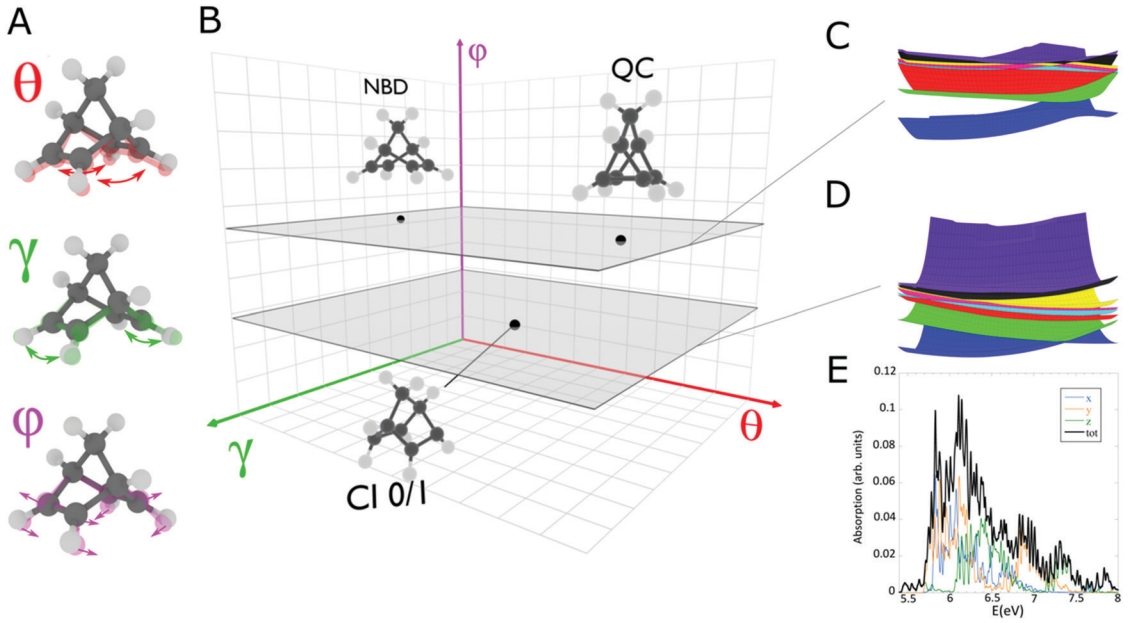

Fig. 2 Coordinates and potential energy surfaces. (A) The three coordinates, θ, γ and φ used to describe the isomerization of norbornadiene to quadricyclane, see Methods and ESI,† Section S1 ande Fig. S1, S2 for more details. The arrows show the displacement of the atoms in the C_4H_4 moiety (the C_3H_4 bridge is kept frozen in the simulations). (B) The grid used in the simulation and the norbornadiene, quadricyclane, and S_0/S_1 conical intersection (CI) geometries on the grid. The planes shown in shaded grey are the $\varphi = 0$ plane that contains the grid point corresponding to the norbornadiene equilibrium geometry and the plane $\varphi = -0.06$ that contains the grid point corresponding to the S_0/S_1 CI. The (C) 2D (θ,γ) cuts in the 3D potential energy surface computed for $\varphi = 0$. In the FC region, the GS remains separated in energy from the excited states. (D) 2D (θ,γ) cuts in the region of the CI seam at $\varphi = -0.06$. The S_0/S_1 CI seam is visible. (E) The absorption spectrum of norbornadiene computed by averaging over the geometries of the wave packet on the ground state using x (blue), y (orange), z (green) polarization. The black line is the sum.

nuclear dimensionality by inferring three coordinates that capture the essence of the ring closure process, in particular the role of the crucial conical intersection (CI) between the ground state S_0 and the lowest excited electronic state, S_1, see Fig. 2. Technical details about the coordinates are given in the ESI,† Section S1 and Fig. S1, S2, and the selected geometries reported in Tables S1–S4. The geometry of the C_3H_4 bridge does not significantly vary between the open and the close forms and was frozen at the equilibrium geometry of norbornadiene, see Fig. S1 (ESI†). Two angles, θ and γ (Fig. 2, panel A), describe the geometry change that accompanies the ring closure. The angle θ essentially corresponds to the symmetric bending mode that modifies the distance between the two ethylene moieties in norbornadiene, see Fig. S2A (ESI†). The angle γ has a high overlap with the stretching mode of the ethylene moieties, see Fig. S2B (ESI†). The modes corresponding to θ and γ are also present in quadricyclane with different frequencies. The ring closure occurs by closing the angle θ and opening the γ one. Then we define a third coordinate, the angle φ, see Fig. S2C (ESI†), that induces a distortion essential to access the geometries where the S_0 and S_1 states are efficiently coupled in the CI region. From these 3 angles, we define a set of 65 000 points at which the molecular electronic structure (energy, transition dipoles and non adiabatic coupling (NAC) for 8 electronic states) is computed (see section Electronic structure below). The data computed at these 65 000 points are then extrapolated over the 492 800 points of the grid to ensure the stability of the wave function on the borders of the grid. More details can be found in Section S3 of the ESI.† The differential operators (kinetic energy and momentum) are represented using the finite-difference method.[18,48] The geometries sampled by the grid have overall a C_2 symmetry, the distortion from C_{2v} being due to the displacements along the φ coordinate. To optimize the computational cost of the dynamics, we limited the extension on the grid on the quadricyclane side so that the grid points do not reach the equilibrium quadricyclane geometry. To avoid non-physical reflections on the boundary of the grid, we used a complex absorbing potential (CAP) on the quadricyclane side. The CAP is placed on grid points in planes (θ, γ) after the CI, for geometries close to that of the quadricyclane, see Fig. S6C (ESI†). Following the dynamics by a fully quantum approach in 3D beyond 200 fs is numerically not stable. The CAP allows monitoring the early time population in the closed form for all electronic states; see details in ESI,† Section S3. During the first 200 fs of the dynamics that could be followed, we do not expect that the use of the CAP masks significant returns of the wave packet form the quadricyclane to the norbornadiene region. The reason is that the components of the wave packet absorbed have momentum towards the quadricyclane region and the potentials on this side are flat. At longer time scales, our reduced system of coordinates does not provide a realistic description of the dynamics. In particular, transfer from excited to lower excited state are expected to be induced by different geometry distortions. Eventually, it is expected that quadricyclane isomerizes back to norbornadiene on the GS the activation barrier about 1.5 eV (see Table S4, ESI†) while it is about

 This journal is © the Owner Societies 2020

Published on 24 September 2020. Downloaded on 1/26/2021 11:44:03 AM.

4.3 eV for the norbornadiene to quadricyclane direction. This asymmetry is exploited in substituted norbornadiene–quadricyclane systems to implement molecular solar-thermal energy storage.[49]

Electronic structure

Computing the coupled electronic-nuclear dynamics on eight coupled electronic states requires the computation of a consistent and accurate electronic structure. Computing such an electronic structure for a tremendous number of molecular geometries, including a significant number of electronic states that are mixed by non-adiabatic couplings, is a daunting task. In particular, the electronic structure of the highly excited states along the norbornadiene to quadricyclane isomerization path is challenging to converge, and a compromise between accuracy and computational efforts has to be made. Potentials energies, transition dipole moments, and non-adiabatic coupling elements are computed for each grid point at the SA(14)-CASSCF(4,8)/AUG-cc-pVDZ level of theory. The OpenMOLCAS software was used throughout.[50] The multi-configuration computation is averaged over a band of 14 electronic states to maximize the consistency of the basis set of 8 electronic states included in the dynamics over the space spanned by the grid. This level of theory provides a trade-off for describing known properties of the norbornadiene/quadricyclane system in the entire grid space, including the norbornadiene and quadricyclane equilibrium geometries, the S_0/S_1 conical intersection (see Fig. 2B), and the low Rydberg and valence states previously reported.[32,47,51] A sketch of the potential energy surfaces is shown in Fig. 2C and D. The symmetries and the energies of the low lying excited states of norbornadiene at its equilibrium geometry obtained at this level of theory on the grid are in reasonable agreement with previous computations[32,47,51] undertaken with different approaches and focusing on a smaller number of excited states and range of geometries. The energetic order of the excited states and their nature is very dependent on the geometry even in the Franck–Condon region because these states are strongly coupled by non-adiabatic interactions. At the SA-CASSF level, only the energy of the valence diffuse B_2 state, which corresponds to excited state S_7, is significantly overestimated at the norbornadiene equilibrium geometry which is of C_{2v} symmetry. The absorption band of this state is weak and very diffuse[51,52] and experimentally challenging to characterize. This suggests that it is accessed on the edges of the Franck–Condon region or at its exit either directly from the ground state because states have different compositions at these geometries and can be accessed through non-adiabatic population transfer from bright states within the Franck–Condon region. The computed absorption spectrum over the Franck–Condon region:

$$S(E) = \int \mathrm{d}E \sum_{i}^{8} \sum_{g \in \mathrm{FC}} \left|\mu_{\mathrm{GS}-i,g}\right|^2 \exp\left(-\frac{\left(E - E_{ig}\right)^2}{2\sigma^2}\right) \qquad (1)$$

with σ = 0.01 eV, is in reasonable agreement (see Fig. 2E) with the experimental ones of ref. 51 and 52. It exhibits sharp progressions of vibrational states superimposed on diffuse bands.

In the Franck–Condon region in the vicinity of the equilibrium geometry, the excited states have definite symmetry properties and are subject to optical selection rules (see Fig. S3, ESI†). It is these optical selection rules in the Franck–Condon region that allow for an efficient tuning of the initial coherent superposition of states using the polarization of the UV pulse. From Fig. S3C (ESI†), one sees that S_1 and S_4 are 3p Rydberg states that belong to the B_1 irreducible representation, lying 5.8 and 6.7 eV above the ground state, respectively. The S_2 state (6.2 eV) is a 3s Rydberg state of A_1 symmetry. The S_0/S_1 and S_0/S_4 transition dipoles, as well as the S_1/S_2 one, are non-zero in the direction perpendicular to the ethylene bonds and parallel to the plane formed by the ethylene bonds (*x*-axis, new bond direction). A polarization along the *z*-axis induces the S_0/S_2 and S_1/S_4 transitions. S_3 (6.3 eV), of mixed valence/Rydberg character, belongs to A_2 and is optically dark. S_5 (7.5 eV) is made of doubly excited configurations and is also optically dark. S_6 (7.6 eV) is a dark mixed valence/Rydberg state of A_2 symmetry. Only the S_7 state, of mixed valence/Rydberg character, belongs to B_2. Excitation energies are reported in Table S4 of the ESI.† The values of the Cartesian components of the transition and permanent dipoles in the space fixed frame shown in the inset of Fig. 1 are given in Table S5 (ESI†).

The non adiabatic coupling (NAC) elements are computed for each pair of electronic states. The NAC region of S_0/S_1 conical intersection that governs the formation of the closed-form on the ground state is well captured by the configurations sampled on the grid, see Fig. S4A and S5A in ESI.† In addition to the S_0/S_1 conical intersection, several others are essential for converting the Rydberg high excited states of norbornadiene to valence states of quadricyclane. Some of these crossing seams, *e.g.* S_2/S_3 and S_3/S_4, are well captured by the three coordinates, resulting in broad regions of coupling across the grid space, see Fig. S4B and S5B of the ESI† for the S_2/S_3 CI seams. Because of the limitations of working in reduced dimensionality, some other CI's, particularly the S_1/S_2 one, are instead characterized by motions that are not well captured by the three coordinates which results in relatively weak couplings in spatially limited regions of the grid space (see Fig. S4C, ESI†). Equilibrium geometries of norbornadiene and quadricyclane are given in Cartesian coordinates in Tables S1 and S2 of the ESI.†

At its equilibrium geometry, the ground state of norbornadiene has a C_{2v} geometry. The permanent dipole moment is non-zero only in the direction perpendicular to the plane of the two ethylene moieties, pointing to the apex C of the frozen C_3H_4 bridge (*z*-axis), see inset in Fig. 1. Its computed value is 0.24 e a_0 (a_0 = 0.529 Å) which supports orienting the molecule in the laboratory frame, shown in the inset in Fig. 1.[53–55]

Results

Control of the ring closure dynamics

The efficiency of the transfer to quadricyclane through the S_1/S_0 CI is very sensitive to the approach angle and the position and momentum of the nuclear wave packet.[56] To clarify the role of

Published on 24 September 2020. Downloaded on 1/26/2021 11:44:03 AM.

the localization of the vibronic wave packet in S_1 around the S_1/S_0 conical intersection seam on the transfer efficiency to the product region, we launched dynamics for five different positions around the S_1/S_0 conical intersection (see ESI,† Section S4, Fig. S6 and S7 for more details). These simulations allowed us to design two pump few-fs UV pulses, one polarized in the x-direction (UV(x)) and one polarized z-direction (UV(z)). Due to optical selection rules in the Franck–Condon region, the UV(x) pulse accesses the S_1 (B_1) Rydberg state. The UV(z) pulse accesses the S_2 (A_1) Rydberg state that is strongly coupled to the S_3 dark state in the Franck–Condon region.

Exciting the oriented molecule by using short pulses of different polarization directions therefore allows us building non stationary electronic densities that are superpositions of electronic states belonging to different irreducible representations of the symmetry group of the nuclear frame. Thereby we induce an initial motion of the electronic density in different spatial directions. We have demonstrated this effect of the polarization of the pulse for the non stationary electronic density computed for frozen nuclei very early on,[57,58] showing that when a superposition of Π and Σ states is built in the LiH molecule, one induces a rotation of the electronic density. When irreducible representation of the excited states allowed by the pulse polarization are not the totally symmetric one of the point group of the nuclear frame, the symmetry of the non stationary density is lower than that of the nuclear frame. This effect has been recently analyzed in ref. 59. As argued in ref. 58, controlling the directionality of the initial motion of the electronic density provides a control on the ensuing nuclear dynamics since the electronic density defines the force on the nuclei. We show here that after a few dozens fs, the coupled electronic-nuclear dynamics that follows the excitation by the UV(z) pulse leads to an initial transfer of population from a region around the S_1/S_0 seam that is more efficient to bring population to the quadricyclane form than the one initiated by the UV(x) pulse. One could try to further optimize the pulses using optimal control or related optimization algorithms.[42,60–63]

We contrast in Fig. 3 the population and coherence dynamics induced by the UV(x) and UV(z) pulses during the first 200 fs of the dynamics. The two pulses have the same carrier frequencies (ω = 6.0 eV) and field strength ($|E| = 0.04E_H/(e\,a_0)$, peak intensity of 5.6×10^{13} W cm^{-2}). $|E|$ is high because the values of the transition dipoles are small, see Tables S5 and S6 (ESI†). The computed field free IP of norbornadiene at the C_{2v} is 8.5 eV. It is therefore expected that significant photoionization does not take place during the pulse. The UV(x) pulse is centered at 10 fs and has a short duration, with a full width at half maximum (FWHM) of 2 fs. It accesses selectively the S_1 state. The ensuing dynamics remains mostly confined to the S_0 and the S_1 states, Fig. 3A. The longer (FWHM = 7.6 fs, centered at 17 fs) UV(z) pulse excites the S_2 Rydberg state with no initial population in S_1 (Fig. 3D). The excitation of the S_2 state initiates rich non-adiabatic dynamics involving the higher Rydberg states S_3 and S_4 before the population is transferred to S_1 from S_2 closer to the product region.

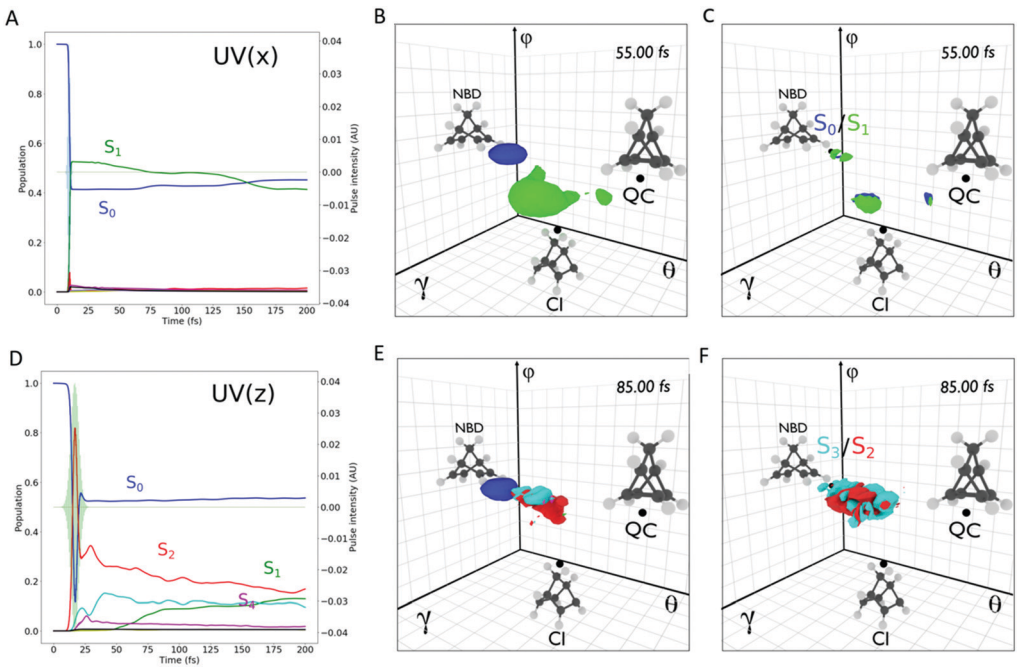

Fig. 3 The UV(x) and UV(z) pulses lead to different dynamics during and after the excitation. The UV(x) pulse (upper row) builds a superposition of S_1 and S_0 in the FC region. The populations are plotted in panel A. The S_0 wave packet remains trapped in the FC region while S_1 travels to the S_0/S_1 CI with essentially no exchange with higher states. At the conical intersection, a S_0/S_1 coherence develops (panel B shows isocontours of the localization in S_0 (blue) and S_1 (green) at 55 fs. Panel C shows an isocontour of the corresponding coherence). The UV(z) pulse (bottom row) builds a coherent superposition of S_0 and S_2 (red) in the Franck–Condon region. The populations are plotted in panel D. S_2 is coupled to S_3 (cyan) by non adiabatic coupling and the S_2/S_3 electronic coherence evolves to the product region. Isocontours of the vibronic S_3/S_2 wave packet localization are plotted in panels E and F; see also Fig. S8 (ESI†) for additional plots of the electronic coherences. Isocontour value: 0.0001 a_0^{-3}.

 This journal is © the Owner Societies 2020

Published on 24 September 2020. Downloaded on 1/26/2021 11:44:03 AM.

The vibronic wave packets built by these pulses evolve to the products along two distinct paths, as shown schematically in Fig. 1. The vibronic wave packet promoted to S_1 by the UV(x) pulse travels to the S_1/S_0 conical intersection region with minimal interactions with the higher excited states. The first transfer through the conical intersection seam occurs at about 55 fs, creating an electronic coherence with S_0 in the product region, (see Fig. 3B and C). Once transferred to S_0, the wave packet can either evolve to the reactant or the product region. The wave packet remaining on S_1 oscillates with a 50 fs period, which corresponds to a complicated motion involving the three coordinates. It revisits the conical intersection region at 100 fs (Fig. S8A, ESI†) and 150 fs (Fig. S8B, ESI†), each time transferring amplitude to S_0, building up S_0/S_1 coherence in this region. On the other hand, the UV(z) pulse excites the S_2 state (Fig. 3D). As it exits the Franck–Condon region, the wave packet in S_2 is rapidly mixed with the S_3 state by non-adiabatic coupling. The S_2/S_3 coherence travels to the product region, continuously exchanging amplitude due to the S_2/S_3 non adiabatic coupling. At 85 fs, the S_2 wave packet reaches the area of weak (because of the reduced dimensionality of the grid used) non adiabatic coupling with the S_1 state building a S_1/S_2 coherence (Fig. S8D, ESI†). Representative isocontours of the S_3/S_2 localization and coherence are shown in Fig. 3E and F, respectively. Here, the nuclear motion involves the θ and φ that describe the ring closure, bringing the electronic density in and out of the double bonds to the new bonds with a period of about 20 fs (see Fig. 4). Then the S_1 wave packet couples to the S_0 state through the S_0/S_1 CI seam (Fig. S8E, ESI† for t = 95 fs).

The different paths followed by the dynamics upon excitation by the UV(x) or the UV(z) lead to different time dependences of the yields in the 'reactant' and 'product'. One can see by comparing Fig. 3C and Fig. S8B and C with Fig. S8E (ESI†) that the S_1 wave packet approaches the S_1/S_0 conical intersection from a different angle for the two excitations. We relate this difference to distinct dynamical behaviors in position and momentum space along the coordinate γ (ethylene stretching). The UV(z) S_1 wave packet forms at relatively small values of γ and the double bond is elongating while the wave packet passes through the seam. In the UV(x) simulation, the S_0/S_1 conical intersection is approached from the other side, when the already elongated double bond starts shortening. By comparing Fig. 3C with Fig. S8D (ESI†), one can see that the positions reached on S_1 by the wave packets initiated by the UV(x) and the UV(z) pulses correspond respectively to initial positions 1 and 4 in Fig. S6 and S7 of the ESI.† After the excitation by the UV(z) pulse, the wave packet reaches a region of the S_1/S_0 conical intersection seam that cannot be explored by the S_1 wave packet produced by the UV(x) pulse. Fig. 4 shows the results of the simulations where the wave packet dynamics is initiated on S_1 at the two positions reached by the UV(x) and the UV(z) dynamics (Fig. 4A) close to the S_0/S_1 conical intersection.

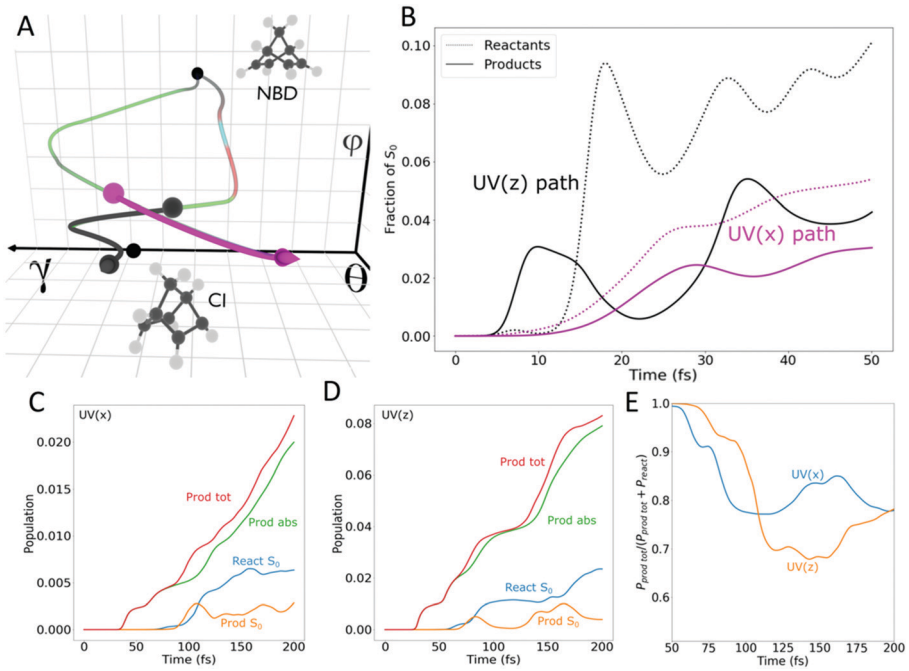

Fig. 4 UV(x) and UV(z) path around the S_0/S_1 conical intersection. Panel (A): Zoom on the mean position of the fraction of the wave packet on S_1 for the two excitations. The UV(x) path is shown in violet and the UV(z) path in dark grey. The two wave packets approach the conical intersection (CI) region with a different angle, which yields a much higher relative amplitude transfer to the product for the UV(z) excitation. Panel (B): Fraction of population on the S_0 state for the product and the reactant resulting from wave packet dynamics started in S_1 at the positions shown in panel (A) (same color code), time = 0 corresponds to the initial positions shown in (A). The angle of approach of the UV(z) pulse leads to a much more efficient amplitude transfer to the quadricyclane form in the first 10 fs. Panels (C) and (D): Population in reactant and product for an excitation by the UV(x) pulse and by the UV(z) one, here time = 0 corresponds to the excitation by the pulse. The yield in product before 50 fs comes from the population in highly excited states that reaches the absorbing potential. Panel (E): The normalized yield in product for the UV(x) and the UV(z) excitation. See also Fig. S6 and S7 (ESI†).

Published on 24 September 2020. Downloaded on 1/26/2021 11:44:03 AM.

The UV(z) position leads to a higher yield and earlier transfer in the product region (Fig. 4B and D). The maximum of transfer occurs about 10 fs after reaching the conical intersection seam in both computations. However, after the first transfer, a significant fraction of the UV(z) wave packet remains trapped on S_2 because our 3D grid does not capture well the region of strong non adiabatic coupling between S_2/S_1. This trapping results in a decreased relaxation to S_1 near the S_1/S_0 conical intersection, which would otherwise yield a higher product selectivity. The wave packet built by UV(x) in S_1 reaches the product region slower because of its momentum and approach angle when funnelling through the conical intersection seam (Fig. 4B and C). We assess the reactant and product yields by partitioning the entire 3D grid in three regions (Fig. S6B, ESI†): a reactant region corresponding to norbornadiene geometries on S_0, a quadricyclane product region on S_0, and an undecided region on S_0. To avoid non-physical reflections on the boundary of the grid, we used a complex absorbing potential (CAP) on the quadricyclane side (Fig. S6C, ESI†). Since the CAP spans the quadricyclane side, we add the total population absorbed to the product. The normalized product yields for the full dynamics are plotted in Fig. 4E. The UV(z) dynamics leads to a higher product yield at early times.

The formation of new bonds

The distinct dynamical paths triggered by the UV(x) and UV(z) excitations lead to different dynamics of the non-stationary electronic density spanning the four carbon atoms involved in the ring closure. At the ground state equilibrium geometries, norbornadiene and quadricyclane have different electronic densities in the 'old' ethylene C–C bonds of norbornadiene and the 'new' C–C bonds formed in quadricyclane. The motions of the electronic density during semibullvalene pericyclic reaction on the ground electronic state for a 1D synchroneous nuclear coordinate have been analyzed using electronic fluxes in ref. 42, 64 and 65. The authors concluded that the electronic density follows a pincer-like motion. For the complex coherent vibronic three dimensional dynamics on several excited states that we investigate here, we adopt a simpler approach. Our analysis therefore does not allow to characterize the motion of the electronic density based on the computation of electronic fluxes. It nevertheless allows us to relate the changes in the overall electronic density in the old and new bonds to the electronic coherences prepared by the UV(x) and UV(z) pulses.

To analyse the electronic density dynamics in the two kinds of bonds, we define non-overlapping cylindric volumes comprising the two C–C bonds for each nuclear grid point (see Fig. 5b, and Section S4.3, ESI†). For an electronic wave packet, the electronic density localized in the bond volumes is a double sum over all the electronic states involved and grid points. The resulting bond density depends on time.

$$\rho^{\mathrm{elec}}_{\mathrm{bond}}(t) = \sum_{i,j}^{N} \sum_{g} c_{ig}{}^{*}(t) c_{jg}(t) \rho^{\mathrm{elec,bond}}_{ij,g} \qquad (2)$$

In eqn (2), i and j stand for electronic states, $i = j$ for stationary densities, and $i \neq j$ for transition ones. We compute the amplitudes $c_{ig}(t)$ by integration of the time-dependent Schrödinger equation. The electronic density in each bond cylinder is calculated as $\rho^{\mathrm{elec,bond}}_{ij,g} = \int_{\text{bond volume}} \rho^{\mathrm{elec}}_{ij,g}(x,y,z)\mathrm{d}x\mathrm{d}y\mathrm{d}z$ where x, y, z are the Cartesian electronic coordinates. The integral is on the volume of the cylinder that encompasses the bond (Fig. 5B). We partition $\rho^{\mathrm{elec}}_{\mathrm{bond}}(t)$ in two terms, the population contribution $\rho^{\mathrm{elec}}_{\text{pop-bond}}(t) = \sum_{i}^{N} \sum_{g} \left|c_{gi}(t)\right|^2 \rho^{\mathrm{elec,bond}}_{ii,g}$ and the coherent contribution $\rho^{\mathrm{elec}}_{\text{coh-bond}}(t) = \sum_{i \neq j}^{N} \sum_{g} c_{gi}{}^{*}(t) c_{gj}(t) \rho^{\mathrm{elec,bond}}_{ij,g}$. The population term depends on the stationary electronic densities, $\rho^{\mathrm{elec,bond}}_{ii,g}$, and reflects the changes in the determinantal composition of the excited states as the wave packet travels on the grid. The coherent contribution depends on the localization of the electronic transition density matrix, $\rho^{\mathrm{elec,bond}}_{ij,g}$, between the two states involved in the coherence.

We show in Fig. 5 the electronic densities in the old and new bonds as a function of time for the two excitations. We normalize the density by the sum over two bond volume at each time to account for the overall decay of electronic density due to the CAP. Unnormalized densities are shown in Fig. S9A and B (ESI†). Before the excitation, the molecules are in the norbornadiene ground state, and there is more density localized in the old bonds than in the new ones. We obtain 3.93 |e| in the old bonds volume and 3.43 |e| in the new bonds volume (Fig. S9A, ESI†). The densities in the two kinds of bonds computed for the equilibrium geometry of the ground state of norbornadiene are 3.8 |e| and 3.2, respectively. As the vibronic wave packet travels to the quadricyclane region, the amount of electron density in the old and the new bonds oscillates. For both paths, the electron density is overall transferred to the new bonds in quadricyclane. At longer times, the electronic density tends to equalize among the two types of bonds.

The period and amplitude of the bonds densities oscillations reflect the distinct dynamics triggered by UV(x) and UV(z). The coherent contribution, $\rho^{\mathrm{elec}}_{\text{coh-bond}}(t)$ is plotted in the top of panels A and D, Fig. 5. The time dependence of the population term, $\rho^{\mathrm{elec}}_{\text{pop-bond}}(t)$, is shown in the corresponding bottom panels. The total density is shown in panel B for a given geometry and the bond volumes in panel C. The coherence term exhibits weak and fast (about 1 fs) oscillations reflecting the coherence between the excited states and the ground state both in the UV(x) and the UV(z) pulses. The population term overall dominates the oscillation of the bond densities. The qualitative difference between the dynamics initiated by the two excitations is that they access different electronic states. The UV(x) pulse (Fig. 5a) produces a wave packet on S_1 and therefore, the amplitude of the coherence is very small since S_1 rapidly exits the Franck–Condon region while the S_0 wave packet remains trapped there. The determinantal composition of S_1 changes drastically as the wave packet travels to the S_0/S_1 region, which is reflected in the population term $\rho^{\mathrm{elec}}_{\text{pop-bond}}(t)$. The first exchange of electronic density between the two kinds of bonds happens at about 40 fs. Just after this exchange,

 This journal is © the Owner Societies 2020

Published on 24 September 2020. Downloaded on 1/26/2021 11:44:03 AM.

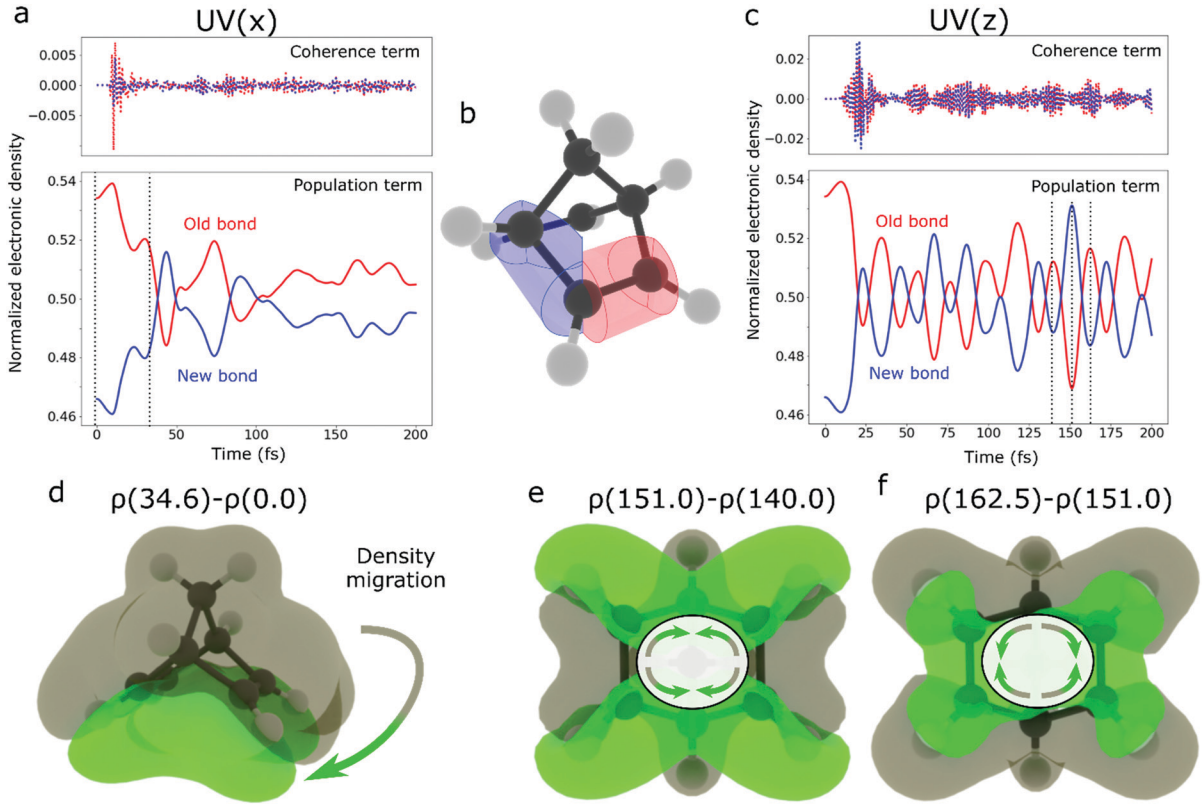

Fig. 5 Time-dependent electronic density (population and coherent contributions) in old (red) and new bonds (blue) for the excitation by the UV(x) (panel a) and the UV(z) (panel d) exciting pulses. An isocontour of the total electronic density is shown in panel b. The volumes of the bonds corresponding to a given geometry are shown in panel c (red cylinder for old bonds and blue cylinder for new ones). Panels e–g: Isocontours of electronic density differences, green: positive, and grey: negative. Panel e: The density difference between the density at 34.6 fs for UV(x) and that of the ground state at time 0 ($\rho^{\mathrm{elec}}_{0\mathrm{fs}}$). Panels f and e correspond to the UV(z) pulse dynamics. Panel f: The change in density for a half period of the population term when the density is migrating to the new bonds so that the density difference is positive (green) in the new bond region and negative (grey) in the new ones. Panel g: The density change when the density is going back to the old bonds. The arrows show the direction of the overall change in the total electronic densities in the old and new bond volumes respectively, as they are reflected by the sign of the density differences between the times indicated in panels e, f and g. They do not represent electronic fluxes. In panels e and f, the nuclear geometries shown are averaged over the wave packet. They belong to the C2 group and the isocontours of density differences to the A irreducible representation of this group.

at 45 fs, density is transferred to the new bonds (Fig. 5e). The determinantal variations result in further exchanges of density between the old and new bonds at around 50 and 100 fs when the S_1 wave packet crosses the S_0/S_1 conical intersection region. In the time range of these crossings, the fast oscillations of the coherent term are modulated by slower oscillations centered at times 40, 70, 90 and 140 fs when the coherence S_0/S_1 is formed. The Fourier transforms of the population and coherence terms are given in Fig. S10C and E (ESI†). The frequency peaks of the population terms at about 0.08 eV for the old bonds and 0.12 for the new ones reflect the slow oscillations. The UV(z) excitation (Fig. 5d) leads to faster (Fig. S10B, ESI†) and more regular beatings of the population term of the electronic density in the bonds than those observed for the UV(x) excitation. The coherent contribution is larger and directly reflects the period of the S_2/S_3 electronic coherence and the motion of the non-equilibrium density. This is confirmed by the isocontour differences of the total electronic density computed for selected times in panels F and G. Panel F corresponds to $\rho^{\mathrm{elec}}_{151\mathrm{fs}} - \rho^{\mathrm{elec}}_{140\mathrm{fs}}$ and panel F $\rho^{\mathrm{elec}}_{162.5\mathrm{fs}} - \rho^{\mathrm{elec}}_{151\mathrm{fs}}$. In panel F, there is an excess of density in the region of the new bonds at t = 151 fs compared to t = 140 fs and *vice versa* at t = 162.5 fs (panel G). These two panels clearly illustrate the electronic density motion in and out of the old and new bonds due to its non-equilibrium character.

Probing of the electronic coherence motion can be achieved by pump–probe fs transient spectroscopy. The linear response transient absorption spectrum[66,67] is given by $S(\omega) = -2\,\mathrm{Im}[\mu(\omega)E^{*}(\omega)]$ where $\mu(\omega)$ is the Fourier transform of the dipole moment, $\mu(t)$, computed for the dynamics including the interaction with the pump and the probe pulses and $E^{*}(\omega)$ is the complex conjugate of the electric field in the frequency domain generated by the two pulses (pump + probe), both computed for positive frequencies, ω. A positive value of the response function, $S(\omega)$, corresponds to an absorption process while a negative value corresponds to emission. $S(\omega)$ is a direct observable of the time-dependent dipole (or time-dependent polarization), $\mu(t)$, also called the total polarization. $\mu(t)$ has three Cartesian components that involve the permanent and transition electric dipoles. Its expression is given in Section S4.4 of

Published on 24 September 2020. Downloaded on 1/26/2021 11:44:03 AM.

the ESI.† Therefore, $\mu(t)$ depends on the stationary and transition one-electron densities, $\rho_{ii}^{\mathrm{elec}}(x,y,z)$ and $\rho_{ij}^{\mathrm{elec}}(x,y,z)$, which appear in the expression of the electronic densities of the new bonds and the old bonds discussed above. The components of the dipole moment are observables of the electronic density and can be used to probe its motion in and out of the C–C during the ring closure. The time dependence of the dipole for the excitation by the two pulses is qualitatively different. We show in Fig. 6 (panels A and B) the three Cartesian components in the laboratory frame of the time-dependent dipole computed for excitation by the UV(x) and UV(z) pulses. For excitation by the UV(x) pulse (Fig. 6A), the x-component of the dipole exhibits very fast oscillations in the Franck–Condon region and after 100 fs. This rapid 1 fs beating (see inset in Fig. 6A) corresponds to the period of the S_0/S_1 electronic coherence present when some S_1 population is localized the Franck–Condon region. The slower modulation corresponds to the coherence between S_1 and S_0 in the conical intersection region and also to coherences of S_1 with higher weakly populated excited states, mainly S_3 and S_4. These appear as low frequencies in the Fourier transform of the dipole, $\mu_x(\omega)$ shown in Fig. S10 of the ESI.† In both UV(x) and UV(z) cases, the magnitude of the dipole moment is the largest along the

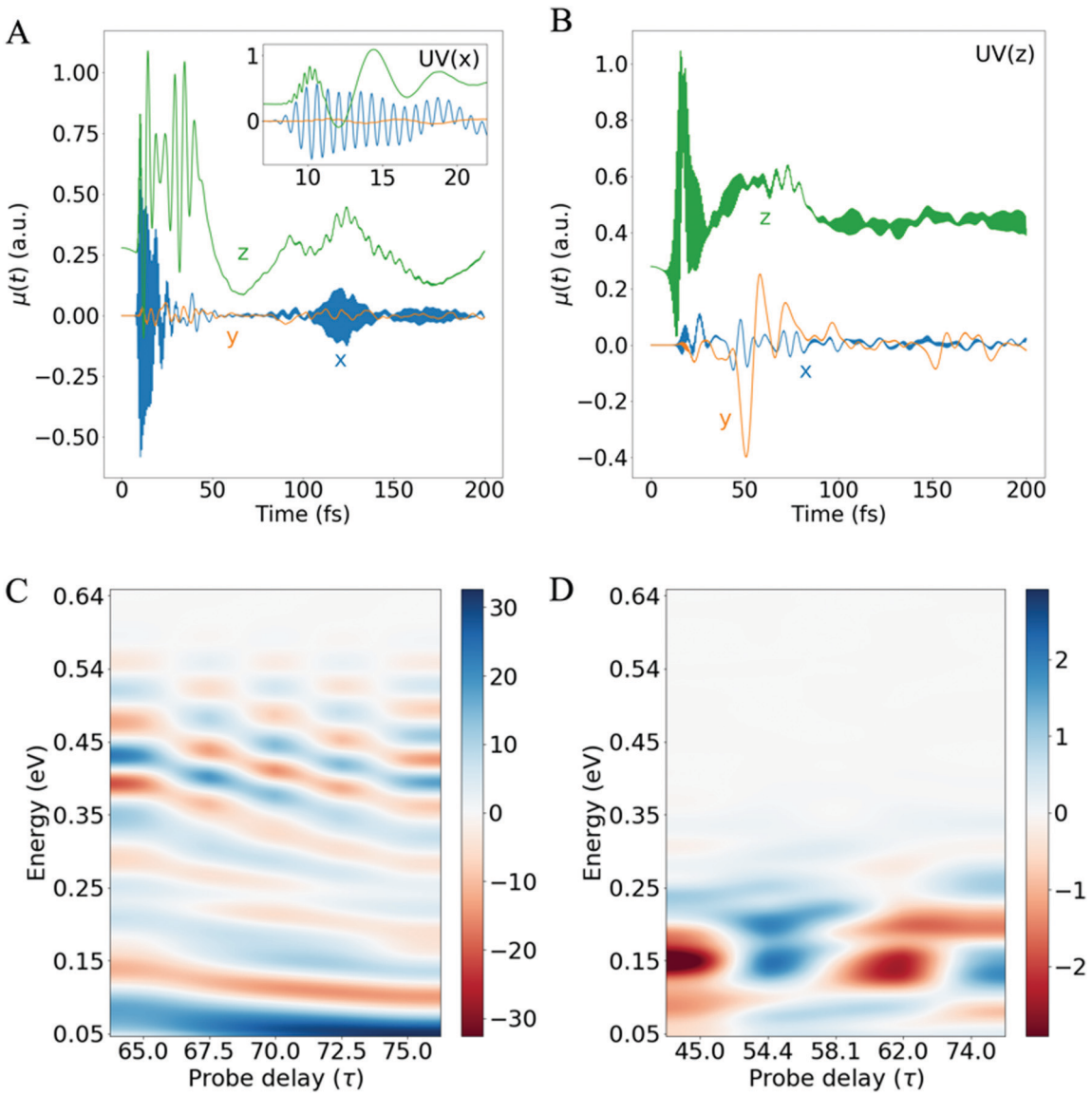

Fig. 6 Time-dependent components of the dipole for excitation by the UV(x) (A) and the UV(z) (B) pulses. Panels C and D: Computed pump–probe transient absorption spectra. The x-axis is the pump–probe delay τ (fs). The y-axis is the frequency range in eV. Panel C: Computed transient absorption spectrum for the UV(x) excitation. The IR probe pulse is polarized along z, and its carrier frequency is tuned to probe the S_0/S_1 coherence built by the passage of the S_1 vibronic wave packet through the S_0/S_1 conical intersection region at 50 fs. In this region, the S_0 and the S_1 states are separated by energy differences of *circa* 0.2 eV that correspond to an oscillation period of 20 fs along the delay time axis (x-axis). The faster oscillations in the 5 fs range seen in the frequency range of 0.4–0.5 eV correspond to the very low amplitude electronic coherence between the S_1 and the S_4 states. Panel D: Computed transient absorption spectrum for the UV(z) excitation. The IR probe pulse is polarized along y and its carrier frequency tailored to probe the S_2/S_3 coherence that has a beating period of *circa* 20 fs.

 This journal is © the Owner Societies 2020

Published on 24 September 2020. Downloaded on 1/26/2021 11:44:03 AM.

z-direction. At early times, between the end of the UV(x) pump pulse (time $\approx$ 12 fs) and the first passage of the S_1 wave packet in the S_0/S_1 region at 50 fs, and to a smaller extent later at 90 and 120 fs, the relatively fast oscillations ranging between 1 and 5 fs are due to the large value of the transition dipole between the S_1 and the S_4 states for the geometries in the S_0/S_1 conical region. The slower modulations of the amplitude are mainly due to the permanent dipole component of S_0 and S_1 along z (first term in eqn (S19) of the ESI†), which is changing because of the geometry changes as the vibronic wave packet passes through the conical region. This slower modulation corresponds to periods of *circa* 20 fs (around 0.2 eV in the Fourier transform spectrum, see Fig. S10 in the ESI†). For the UV(x) pulse, the y component of the dipole remains small during the entire dynamics.

For an excitation by the UV(z) pulse, the dipole along x is very small because there is virtually no population in S_1 during the dynamics. On the other hand, there is a relatively large component along y that, by analyzing the different contributions of the excited states (see ESI,† Section S4.3), we can ascribe to the S_2/S_3 coherence. The corresponding frequencies in the Fourier transform vary between 0.02 and 0.5 eV that correspond to the S_2–S_3 energy differences in the region of the coherence and to the frequencies obtained by taking the Fourier transform of the oscillations of the electronic density in and out the old and the new bonds, see Fig. S9 in the ESI.† The z-component at around 6 eV is much larger than the other two because the pulse is polarized along z and excites states with a high transition dipole in this direction. The fast *circa* 1 fs oscillation corresponds to the 6 eV difference between the ground state and S_2 in the Franck–Condon region. This component is absent from the UV(x) excitation dynamics. Similar to the UV(x) dynamics, the slower periods of the oscillations of the z-component are due to the S_1/S_4 coherence and to the changes of the S_0 and the S_2 permanent dipoles with the geometries spanned by the vibronic wave packet as it evolves in the conical intersection regions.

The analysis of the time-dependence and the frequency spectrum of the dipole moment components suggests that it is possible to monitor the electronic coherences by fs pump–probe transient absorption spectroscopy. For the UV(x) excitation, the S_1/S_0 coherence created by the passage of the S_1 wave packet in the S_0/S_1 conical intersection region can be probed by a short few-cycle IR pulse linearly polarized in the z-direction. We show the pump–probe transient absorption spectrum in Fig. 6C. The frequency of the probe IR pulse is 0.4 eV, its FWHM 8.5 fs (bandwidth of 0.48 eV) and its strength $0.01E_H/e\ a_0$. Because of the continuous variations in the S_0–S_1 energy difference in the conical intersection region in this time range and of the change in the dipoles due to the geometry changes, the period of the oscillations are not well defined, but half a period of the oscillation of the S_1/S_0 coherence is clearly visible in the 0.15–0.25 frequency range, which is confirmed by plotting the transient absorption corresponding solely to off-diagonal S_1/S_0 transition dipole term (see Fig. S10C in the ESI†). On the other hand, the S_2/S_3 coherence can be probed by a few-cycle IR pulse polarized along y (field strength $0.0005E_H/e\ a_0$, frequency 0.27 eV, FWHM = 11.3 fs, energy bandwidth 0.3 eV), Fig. 6D. In that case, the 20 fs oscillation period is much better resolved, as can be inferred from the oscillation of the dipole along y shown in Fig. 6B. The transient absorption spectrum is dominated by the contribution of the S_2/S_3 transition dipole, as can be seen from Fig. S10D of the ESI.† The oscillations probed in the transient absorption spectrum can be directly related to the oscillation density of the electronic density in and out of the bonds shown in Fig. 5.

Conclusions

We undertook this study to show that ultrafast light-induced processes can not only break but also make bonds. Our example is norbornadiene, which can undergo a four center ring closure. Norbornadiene exhibits a high density of strongly interacting electronic states of Rydberg and mixed valence/Rydberg character from about 6 eV above the ground state. Our quantum dynamical results show that in the first 200 fs different pathways of the ring closure from norbornadiene to quadricyclane can be triggered by initiating markedly different non-stationary electronic densities in the Franck–Condon region using short few fs UV pulses of different polarization. The control results from the different characters of the optically bright low lying Rydberg states that can be optically accessed. A short 2 fs UV pulse polarized along x accesses selectively a B_1 Rydberg state (S_1) optically bright along x while a slightly longer UV pulse polarized along z selectively excites an A_1 Rydberg (S_2) optically active along z. The A_1 S_2 state is strongly coupled by non-adiabatic interactions with the mixed Rydberg/valence A_2 S_3 state that is dark at the norbornadiene equilibrium geometry. In the case of the UV(z) excitation, the non-equilibrium electronic density is already a S_2/S_3 electronic coherence in the Franck–Condon region. As the S_2/S_3 wave packet evolves, new electronic coherences appear between S_2 and S_1 due to non-adiabatic interactions. This specific path brings the wave packet on S_1 to the S_0/S_1 conical intersection region from an angle that leads to a high transfer to the quadricyclane region on the S_0 state. On the other hand, the S_1 wave packet produced by the UV(x) excitation remains decoupled from higher electronic states during the entire dynamics. Its path in the S_0/S_1 conical region leads to higher yields in norbornadiene on S_0. *In silico*, the motion of the electronic density out of the old and into the new C–C bonds can be probed by fs pump–probe transient absorption spectroscopy.

The electronic structure of the norbornadiene–quadricyclane system is very complex because of the high density of electronic states of mixed Rydberg/valence character. Our study shows that this complexity is a key for efficiently controlling its reactivity based on the features of the initial non-equilibrium electronic density and the ensuing coherent vibronic dynamics. An accurate description of the coherent electronic-nuclear dynamics requires a fully quantum dynamical description with the unavoidable drawback of having to work in reduced nuclear dimensionality and being limited to the first few hundred

femtosecond dynamics. Longer time dynamical simulations in full dimensionality would be necessary to follow the reaction all the way to the quadricyclane product. It is however expected that the nuclear motion does not explore all the available degrees of freedom in a few hundreds of fs.[68] Our study shows that in this early, few hundreds of fs time regime, it is the coupling between electronic degrees of freedom that is essential and that control can be achieved by exploiting it.[6,69–71]

Conflicts of interest

There are no conflicts to declare.

Acknowledgements

This work was supported by the Fonds National de la Recherche Scientifique (Belgium), F.R.S.-FNRS research grants #T.0132.16 and #J.0012.18 and the AMOS program within the Chemical Sciences, Geosciences and Biosciences Division of the Office of Basic Energy Sciences, Office of Science, US Department of Energy, Award #DE-SC0012628. Computational resources have been provided by the Consortium des Equipements de Calcul Intensif (CECI), funded by the F.R.S.-FNRS under Grant #2.5020.11. SvdW thanks FRS-FNRS for a PhD fellowship. We thank Raphael Levine for discussions about dynamics, Ignacio Fernandez Galvan for useful advices for exploiting the electronic structure outputs of the OpenMOLCAS software, Sebastian Mai and Leticia Gonzales for advices regarding the phase sign correction of the wave function in OpenMOLCAS.

Published on 24 September 2020. Downloaded on 1/26/2021 11:44:03 AM.

References

1 P. B. Corkum and F. Krausz, *Nat. Phys.*, 2007, **3**, 381–387.
2 E. Goulielmakis, M. Schultze, M. Hofstetter, V. S. Yakovlev, J. Gagnon, M. Uiberacker, A. L. Aquila, E. M. Gullikson, D. T. Attwood, R. Kienberger, F. Krausz and U. Kleineberg, *Science*, 2008, **320**, 1614–1617.
3 M. Nisoli, S. De Silvestri, O. Svelto, R. Szipöcs, K. Ferencz, C. Spielmann, S. Sartania and F. Krausz, *Opt. Lett.*, 1997, **22**, 522–524.
4 C. G. Durfee, S. Backus, H. C. Kapteyn and M. M. Murnane, *Opt. Lett.*, 1999, **24**, 697–699.
5 V. Wanie, M. Galli, E. P. Månsson, M. C. Castrovilli, F. Légaré, F. Frassetto, L. Poletto, M. Nisoli and F. Calegari, Conference on Lasers and Electro-Optics, San Jose, California, 2018.
6 F. Remacle and R. D. Levine, *Proc. Natl. Acad. Sci. U. S. A.*, 2006, **103**, 6793–6798.
7 F. Calegari, G. Sansone, S. Stagira, C. Vozzi and M. Nisoli, *J. Phys. B: At., Mol. Opt. Phys.*, 2016, **49**, 062001.
8 P. M. Kraus, B. Mignolet, D. Baykusheva, A. Rupenyan, L. Horný, E. F. Penka, G. Grassi, O. I. Tolstikhin, J. Schneider, F. Jensen, L. B. Madsen, A. D. Bandrauk, F. Remacle and H. J. Wörner, *Science*, 2015, **350**, 790–795.
9 M. Nisoli, P. Decleva, F. Calegari, A. Palacios and F. Martín, *Chem. Rev.*, 2017, **117**, 10760–10825.
10 *Attosecond molecular dynamics*, ed. M. J. J. Vrakking and F. Lepine, The Royal Society of Chemistry, Cambridge, 2019.
11 M. F. Kling, C. Siedschlag, A. J. Verhoef, J. I. Khan, M. Schultze, T. Uphues, Y. Ni, M. Uiberacker, M. Drescher, F. Krausz and M. J. J. Vrakking, *Science*, 2006, **312**, 246–248.
12 W. Li, A. A. Jaron-Becker, C. W. Hogle, V. Sharma, X. Zhou, A. Becker, H. C. Kapteyn and M. M. Murnane, *Proc. Natl. Acad. Sci. U. S. A.*, 2010, **107**, 20219–20222.
13 F. Calegari, D. Ayuso, A. Trabattoni, L. Belshaw, S. De Camillis, S. Anumula, F. Frassetto, L. Poletto, A. Palacios, P. Decleva, J. B. Greenwood, F. Martín and M. Nisoli, *Science*, 2014, **346**, 336–339.
14 C. Neidel, J. Klei, C. H. Yang, A. Rouzée, M. J. J. Vrakking, K. Klünder, M. Miranda, C. L. Arnold, T. Fordell, A. L'Huillier, M. Gisselbrecht, P. Johnsson, M. P. Dinh, E. Suraud, P. G. Reinhard, V. Despré, M. A. L. Marques and F. Lépine, *Phys. Rev. Lett.*, 2013, **111**, 033001.
15 W. K. Peters, D. E. Couch, B. Mignolet, X. Shi, Q. L. Nguyen, R. C. Fortenberry, H. B. Schlegel, F. Remacle, H. C. Kapteyn, M. M. Murnane and W. Li, *Proc. Natl. Acad. Sci. U. S. A.*, 2017, **114**, E11072–E11081, DOI: 10.1073/pnas.1712566114.
16 A. Nikodem, R. D. Levine and F. Remacle, *Phys. Rev. A*, 2017, **95**, 053404.
17 S. van den Wildenberg, B. Mignolet, R. D. Levine and F. Remacle, *J. Chem. Phys.*, 2019, **151**, 134310.
18 S. A. Jayantha, K. G. Komarova, S. v. d. Wildenberg, F. Remacle and R. D. Levine, in *Attosecond Molecular Dynamics*, ed. M. J. J. Vrakking and F. Lepine, Royal Society of Chemistry, Cambridge, 2018, vol. 13, pp. 308–347.
19 R. B. Woodward and R. Hoffmann, *The conservation of orbital symmetry*, Verlag Chemie, Weinheim, 1971.
20 *Excited States of Organic Molecules*, ed. M. Klessinger and J. Michl, VCH Publisher, New York, 1995.
21 P. Vogel and K. H. Houk, *Organic Chemistry: Theory, Reactivity and Mechanisms in Modern Synthesis*, Wiley-VCH, Weinheim, 2019.
22 F. Bernardi, M. Olivucci and M. A. Robb, *Chem. Soc. Rev.*, 1996, **25**, 321–328.
23 *Computational Photochemistry*, ed. M. Olivucci, Elsevier, Amsterdam, 2005.
24 *Conical Intersections: Theory, Computations, Experiments*, ed. W. Domcke, D. R. Yarkony and H. Köppel, World Scientific, Singapore, 2011.
25 S. De Feyter, E. W. G. Diau and A. H. Zewail, *Femtochemistry*, 2001, 97–112.
26 E. W. G. Diau, S. De Feyter and A. H. Zewail, *Chem. Phys. Lett.*, 1999, **304**, 134–144.
27 B. A. Horn, J. L. Herek and A. H. Zewail, *J. Am. Chem. Soc.*, 1996, **118**, 8755–8756.
28 S. Pedersen, J. L. Herek and A. H. Zewail, *Science*, 1994, **266**, 1359.
29 A. H. Zewail, *Femtochemistry: Ultrafast Dynamics of the Chemical Bond*, World Scientifc, Singapore, 1994.
30 W. Fuß, S. Lochbrunner, A. M. Müller, T. Schikarski, W. E. Schmid and S. A. Trushin, *Chem. Phys.*, 1998, **232**, 161–174.

 This journal is © the Owner Societies 2020

Published on 24 September 2020. Downloaded on 1/26/2021 11:44:03 AM.

31 W. Fuß, W. E. Schmid and S. A. Trushin, *J. Chem. Phys.*, 2000, **112**, 8347–8362.
32 W. Fuß, K. K. Pushpa, W. E. Schmid and S. A. Trushin, *Photochem. Photobiol. Sci.*, 2002, **1**, 60–66.
33 F. Rudakov and P. M. Weber, *J. Chem. Phys.*, 2012, **136**, 134303.
34 G. A. Worth, M. J. Bearpark and M. A. Robb, in *Theoretical and Computational Chemistry*, ed. M. Olivucci, Elsevier, 2005, vol. 16, pp. 171–190.
35 M. Boggio-Pasqua, M. Ravaglia, M. J. Bearpark, M. Garavelli and M. A. Robb, *J. Phys. Chem. A*, 2003, **107**, 11139–11152.
36 I. Polyak, L. Hutton, R. Crespo-Otero, M. Barbatti and P. J. Knowles, *J. Chem. Theory Comput.*, 2019, **15**, 3929–3940.
37 M. Assmann, H. Köppel and S. Matsika, *J. Phys. Chem. A*, 2015, **119**, 866–875.
38 M. Ben-Nun and T. J. Martínez, *J. Am. Chem. Soc.*, 2000, **122**, 6299–6300.
39 T. Mori, W. J. Glover, M. S. Schuurman and T. J. Martinez, *J. Phys. Chem. A*, 2012, **116**, 2808–2818.
40 T. J. A. Wolf, D. M. Sanchez, J. Yang, R. M. Parrish, J. P. F. Nunes, M. Centurion, R. Coffee, J. P. Cryan, M. Gühr, K. Hegazy, A. Kirrander, R. K. Li, J. Ruddock, X. Shen, T. Vecchione, S. P. Weathersby, P. M. Weber, K. Wilkin, H. Yong, Q. Zheng, X. J. Wang, M. P. Minitti and T. J. Martínez, *Nat. Chem.*, 2019, **11**, 504–509.
41 M. Saab, L. J. Doriol, B. Lasorne, S. Guérin and F. Gatti, *Chem. Phys.*, 2014, **442**, 93–102.
42 T. Bredtmann and J. Manz, *J. Chem. Sci.*, 2012, **124**, 121–129.
43 A. Hofmann and R. de Vivie-Riedle, *J. Chem. Phys.*, 2000, **112**, 5054–5059.
44 A. Hofmann and R. de Vivie-Riedle, *Chem. Phys. Lett.*, 2001, **346**, 299–304.
45 J. B. Schönborn, J. Sielk and B. Hartke, *J. Phys. Chem. A*, 2010, **114**, 4036–4044.
46 R. D. Bach, I. L. Schilke and H. B. Schlegel, *J. Org. Chem.*, 1996, **61**, 4845–4847.
47 I. Antol, *J. Comput. Chem.*, 2013, **34**, 1439–1445.
48 K. G. Komarova, F. Remacle and R. D. Levine, *Mol. Phys.*, 2018, **116**, 2524–2532.
49 J. Orrego-Hernández, A. Dreos and K. Moth-Poulsen, *Acc. Chem. Res.*, 2020, **53**, 1478–1487, DOI: 10.1021/acs.accounts.1020c00235.
50 I. F. Galván, M. Vacher, A. Alavi, C. Angeli, F. Aquilante, J. Autschbach, J. J. Bao, S. I. Bokarev, N. A. Bogdanov, R. K. Carlson, L. F. Chibotaru, J. Creutzberg, N. Dattani, M. G. Delcey, S. S. Dong, A. Dreuw, L. Freitag, L. M. Frutos, L. Gagliardi, F. Gendron, A. Giussani, L. González, G. Grell, M. Guo, C. E. Hoyer, M. Johansson, S. Keller, S. Knecht, G. Kovačević, E. Källman, G. Li Manni, M. Lundberg, Y. Ma, S. Mai, J. P. Malhado, P. Å. Malmqvist, P. Marquetand, S. A. Mewes, J. Norell, M. Olivucci, M. Oppel, Q. M. Phung, K. Pierloot, F. Plasser, M. Reiher, A. M. Sand, I. Schapiro, P. Sharma, C. J. Stein, L. K. Sørensen, D. G. Truhlar, M. Ugandi, L. Ungur, A. Valentini, S. Vancoillie, V. Veryazov, O. Weser, T. A. Wesołowski, P.-O. Widmark, S. Wouters, A. Zech, J. P. Zobel and R. Lindh, *J. Chem. Theory Comput.*, 2019, **15**, 5925–5964.
51 B. O. Roos, M. Merchan, R. McDiarmid and X. Xing, *J. Am. Chem. Soc.*, 1994, **116**, 5927–5936.
52 X. Xing, A. Gedanken, A.-H. Sheybani and R. McDiarmid, *J. Phys. Chem.*, 1994, **98**, 8302–8309.
53 O. Ghafur, A. Rouzee, A. Gijsbertsen, W. K. Siu, S. Stolte and M. J. J. Vrakking, *Nat. Phys.*, 2009, **5**, 289–293.
54 P. M. Kraus, O. I. Tolstikhin, D. Baykusheva, A. Rupenyan, J. Schneider, C. Z. Bisgaard, T. Morishita, F. Jensen, L. B. Madsen and H. J. Wörner, *Nat. Commun.*, 2015, **6**, 7039.
55 H. Stapelfeldt and T. Seideman, *Rev. Mod. Phys.*, 2003, **75**, 543–557.
56 K. G. Komarova, S. van den Wildenberg, F. Remacle and R. D. Levine, *J. Phys. B: At., Mol. Opt. Phys.*, 2020, **53**, 134001, DOI: 10.1088/1361-6455/ab84c7.
57 F. Remacle, R. Kienberger, F. Krausz and R. D. Levine, *Chem. Phys.*, 2007, **338**, 342–347.
58 F. Remacle, M. Nest and R. D. Levine, *Phys. Rev. Lett.*, 2007, **99**, 183902.
59 D. Haase, J. Manz and J. C. Tremblay, *J. Phys. Chem. A*, 2020, **124**, 3329–3334.
60 P. v. d. Hoff, S. Thallmair, M. Kowalewski, R. Siemering and R. d. Vivie-Riedle, *Phys. Chem. Chem. Phys.*, 2012, **14**, 14460–14485.
61 S. A. Rice and M. Zhao, *Optimal Control of Molecular Dynamics*, Wiley & Sons, New York, 2000.
62 M. Shapiro and P. Brumer, *Quantum control and molecular processes*, Wiley-VCH, Weinheim, 2012.
63 B. Y. Chang, S. Shin and I. R. Sola, *J. Phys. Chem. Lett.*, 2015, **6**, 1724–1728.
64 T. Bredtmann, H. Kono, J. Manz, K. Nakamura and C. Stemmle, *ChemPhysChem*, 2013, **14**, 1397–1404.
65 T. Bredtmann and J. Manz, *Angew. Chem., Int. Ed.*, 2011, **50**, 12652–12654.
66 L. Seidner, G. Stock and W. Domcke, *J. Chem. Phys.*, 1995, **103**, 3998–4011.
67 W. Mengxi, C. Shaohao, C. Seth, J. S. Kenneth and B. G. Mette, *J. Phys. B: At., Mol. Opt. Phys.*, 2016, **49**, 062003.
68 F. Remacle and R. D. Levine, *J. Phys. Chem.*, 1991, **95**, 7124–7127.
69 R. Weinkauf, P. Schanen, A. Metsala, E. W. Schlag, M. Buergle and H. Kessler, *J. Phys. Chem.*, 1996, **100**, 18567–18585.
70 R. Weinkauf, E. W. Schlag, T. J. Martinez and R. D. Levine, *J. Phys. Chem. A*, 1997, **101**, 7702–7710.
71 F. Remacle, R. D. Levine, E. W. Schlag and R. Weinkauf, *J. Phys. Chem. A*, 1999, **103**, 10149–10158.